Doppler and Angle of Arrival Estimation from Digitally Modulated Satellite Signals in Passive RF Space Domain Awareness

Mohd Noor Islam, Thomas Q. Wang, Samuel Wade, Travis Bessell, Tim Spitzer, Jeremy Hallett

Clearbox Systems Pty. Ltd., ACT, Australia.
sda@clearboxsystems.com.au

ABSTRACT

Space Domain Awareness (SDA) or Space Situational Awareness (SSA) is crucial for maintaining custody of satellites especially as the number of active satellites continues to increase rapidly. Passive Radio Frequency (RF) is a promising technique that compliments traditional SDA sensors, including RADARs and telescopes. Passive RF sensors can operate 24/7 in all weather conditions detecting transmissions from satellites across all orbital regimes. In a Passive RF system, Doppler and Angle of Arrival (AoA) can be estimated from the received satellite signal. Satellites transmit payload or Telemetry, Tracking and Command (TT&C) data using different modulation techniques, such as Amplitude Shift Keying (ASK), Phase Shift Keying (PSK) and Frequency Shift Keying (FSK). The different modulation techniques, combined with various line encoding, makes accurate Doppler and AoA estimation challenging. This paper describes and implements a new technique based on Welch's Power Spectral Density (PSD) method to estimate the Doppler for a variety of modulated real satellite signals. The estimated Doppler is compared to both Two Line Element (TLE) sets published by the 18th Space Control Squadron (18SPCS) and accurate International Laser Ranging Service (ILRS) ephemeris data published by Crustal Dynamics Data Information System (CDDIS). This paper also proposes an L-shaped planar antenna array to apply both the interferometer method and the well-known Multiple Signal Classification (MUSIC) algorithm for AoA estimation. The AoA estimation is carried out for an ASK modulated real satellite signal and compared against TLEs.

Keywords: Space Domain Awareness (SDA), Doppler, Angle of Arrival (AoA), Passive Radio Frequency (RF)

1. INTRODUCTION

Space assets are crucial to defence and civilian operations including weather monitoring, communications, and positioning, navigation, and timing (PNT). In recent years, low cost of launch and the competition in private industries on service-centred satellite constellations has caused space to become very congested, contested, and competitive. For example, the enhancement of ridesharing capability has allowed a record breaking 143 spacecraft to be launched by a single Falcon 9 rocket in 2021 with the previous record being 104 spacecraft by an Indian PSLV rocket in 2017 [1], It is predicted that there will be about 50,000 satellites in space by the end of the next decade [2]. Therefore, increased risk of collisions and a high threat posture between state actors, who want to leverage space, are two main challenges to service providers soon and raises severe concern around Space Traffic Management (STM).

Space Domain Awareness (SDA) or Space Situational Awareness (SSA) provides a foundation for all space doctrine, from protecting and defending space-based capabilities, to de-conflicting space traffic, to battle damage assessment. These operations require accurate and timely SDA including reliable detection of objects and determination of the intent of their activities to identify collision risks and threats. To date, SDA is primarily enabled by ground-based radar, optical telescopes, and Satellite Laser Ranging (SLR). Current SDA platforms are incapable of handling the future demand of uninterrupted monitoring due to their limitations. Ground-based RADAR technology is mainly limited to Low Earth Orbit (LEO) and can only be extended at great cost. Optical telescopes and SLR are limited by cloudy/rainy weather and/or daylight. Therefore, the SDA mission faces challenges for achieving 24/7 surveillance.

Passive Radio Frequency (RF) sensing technology for SDA leverages the transmitted signal from the satellite to determine the satellite attributes and attitudes. RF spectrum monitoring and interference detection for satellite communication technology is matured and has been a common practice for many years. Depending on the transmission

frequency, satellite emissions are not substantially affected by weather or the time of day. Passive RF technology can detect satellites at any range, so long as the satellite is transmitting over the area where a sensor is located. However, passive RF sensors can only detect active satellites and therefore, passive RF technology can complement existing SDA sensors in achieving an uninterrupted 24/7 surveillance in all weather conditions. Passive RF sensing can also assist with identification of satellites based on their unique transmissions to prevent the cross-tagging problem that can occur in traditional SDA sensors.

United States (US) based company, Kratos, has demonstrated passive RF technology through the repurposing of their existing RF sensors to provide SDA monitoring for active satellites. The research has highlighted Passive RF's capability in determining GEO satellite manoeuvres [3,4,5]. In Europe, companies such as Zodiac GmbH and Siemens AG are similarly looking to use their RF networks for SDA [6,7]. In Australia, the Murchison Widefield Array (MWA), a precursor for the Square Kilometre Array (SKA) [8] mainly used for astrophysics and space weather, tested an option of passive RF detection in 2015. Orbit determination of a LEO satellite using passive RF is still challenging since they are only observable from a single ground location for a short period of time and often are only transmitting intermittently. Passive RF sensors can generate observations on satellites in the form of Doppler [9], Angle of Arrival (AoA), Time Difference of Arrival (TDoA) and Frequency Difference of Arrival (FDoA). These observations can be used to estimate/infer aspects of the satellite such as determining its orbit.

Doppler is defined as the difference between observed and transmitted carrier frequencies. Satellite transmissions includes Telemetry, Tracking and Command (TT&C) data and payload data such as communications, imagery, etc. These transmissions may use different modulation techniques, such as Amplitude Shift Keying (ASK), Frequency Shift Keying (FSK), Phase Shift Keying (PSK), etc. Different line coding techniques are also used to accommodate both payloads and protocol signals in the approved frequency band. For example, SARAL uses BPSK with Manchester line coding to accommodate PMT-A3 in the middle of the frequency band [10]. Again, CAS-4A uses A.25 protocol signal in the middle of the two FSK carriers. PSK modulated signals span a spread of frequencies. Therefore, it's challenging to determine the true carrier frequency to estimate the Doppler.

This paper describes a new technique based on Welch's Power Spectral Density (PSD) method [11] to estimate the Doppler for a variety of modulated signals. Real data from satellites covering various modulated signals were captured using Clearbox Systems' Passive RF sensing network to verify the technique. The results were compared to both Two Line Element (TLE) sets published by the 18th Space Control Squadron (18SPCS) [12] and accurate International Laser Ranging Service (ILRS) ephemeris data published by Crustal Dynamics Data Information System (CDDIS) [13].

Angle of Arrival (AoA) or Direction Finding (DF) is a common operation that is performed when detecting RF signals in an antenna array [14]. Applying these techniques to satellite transmissions is challenging due to the faint signal strength and intermittent transmissions. Using a low-cost L-shaped spatial planar array of three omni directional antennas, it is possible to estimate the AoA of Low Earth Orbit (LEO) satellites as they pass overhead. Two techniques including the interferometer method and the well-known Multiple Signal Classification (MUSIC) algorithm were employed and compared. These techniques were applied to a satellite that was transmitting an ASK modulated signal.

The following section outlines the passive RF sensing system. In section 3, the Doppler and the angle of arrival (AoA) estimation techniques are explained. Section 4 provides an overview of the passive RF sensors used to collect real satellite data. Section 5 highlights the estimated Doppler and AoA results for real satellite data and the paper is concluded in section 6.

2. PASSIVE RF SYSTEM

A typical Passive RF system consists of RF antennas/sensors, a signal digitisation unit, and a data processing unit as presented in the block diagram shown in Fig. 1. Satellites make use of a wide range of frequencies bands from 30 MHz (VHF-band) to 40 GHz (Ka-band) and beyond.

The capability of a passive RF system is limited by the RF sensor/antenna selection in the RF frontend. Directional antennas and motorised rotors can be used to receive signals with high gain, at the expense of having a narrower field of view. Alternatively, omni-directional antennas can be used to sense satellite signals in a wide field of view but with reduced capacity to sense lower power signals. Narrow band antennas have a higher probability to detect signals in

areas with greater electromagnetic noise. Careful geographical placement of RF sensors can reduce noise and allow wideband antennas to be used effectively to sense a wider variety of satellites, thereby reducing the cost to satellite coverage ratio.

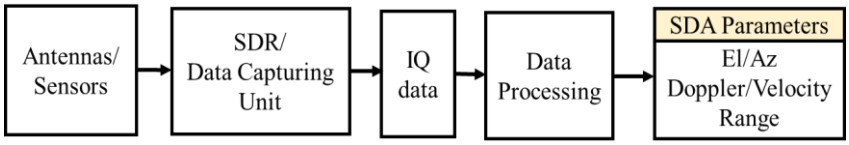

Fig. 1:Block Diagram for a Passive RF sensing system

The next important part of the passive RF system is the digitiser. Software Defined Radios (SDRs) are commonly used to digitise RF signals as in-phase and quadrature components referred to as IQ data. The IQ data is then processed in a Central Processing Unit (CPU)/Graphics Processing Unit (GPU) to extract information from the data. Data processing complexity can be minimised when the signal capturing bandwidth is minimised and by distributing the total band of interest in to different SDR channels. The SDA parameters including Doppler, Azimuth, Elevation, Time Difference of Arrival (TDoA) and Frequency Difference of Arrival (FDoA) can be estimated from the IQ data.

3. DOPPLER AND ANGLE OF ARRIVAL

Satellites transmit data using various modulation techniques, such as ASK, FSK and PSK. The frequency spectrum of received satellite signals are shown in Fig. 2 in green, which are (a) ASK modulated/CW signal from Max Valier Sat, (b) GMSK modulated signal A.25 protocol signal in the middle of the FSK carriers transmitted from CAS-4A and (c) BPSK signal transmitted by JY1SAT. SDA parameters such as Doppler and AoA are estimated based on the received satellite signal and prior information of the satellite transmitter. Doppler estimation requires estimation of the carrier frequency which is challenging due to the different modulation types. On the other hand, AoA estimation requires signals from an array of antennas. Doppler and AoA estimation techniques are explained in this section.

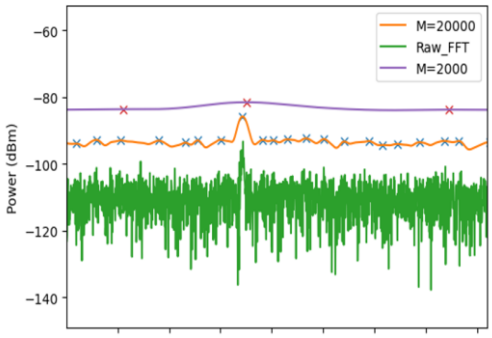

(a) ASK Signal (Max Valier Sat)

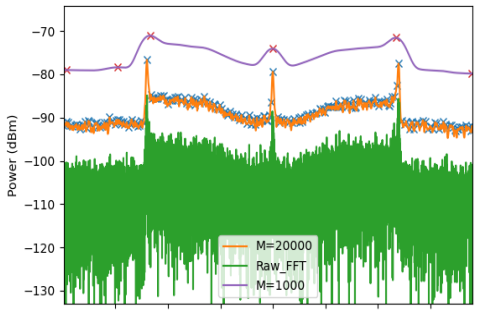

(b) GFSK A.25 signal (CAS-4A)

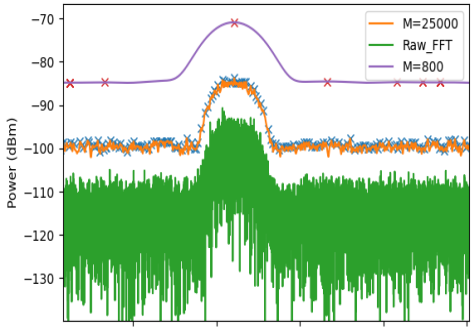

(c) BPSK signal (JY1SAT)

Fig. 2. FFT of various modulated signals and their power spectral density by Welch method.

3.1 Doppler Analysis:

The Doppler frequency or Doppler shift is the difference between the transmitted and observed frequency,

$$f_d = f_o - f_t, \tag{1}$$

where, f_d is the Doppler frequency, f_t is the satellite transmitter frequency, and f_o is the observed frequency. Since the transmitted frequency f_t is to be known, the Doppler shift depends on the accurate determination of the observed frequency. In this paper, a generic method to determine the observed frequency f_o of different modulated signals is proposed. The method uses Welch method to smooth the frequency spectrum followed by a peak finding algorithm determine the observed frequency. The frequency band can be represented by a single peak when the design parameters of the Welch method is appropriately chosen.

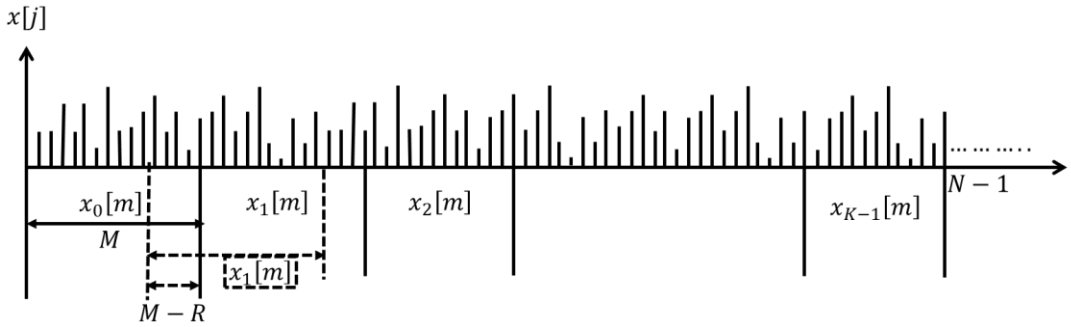

Fig. 3. Welch Method analysis

Welch method [11] is a well-known technique that estimates the power spectral density by dividing the time signal into successive blocks, forming the periodogram for each block, and then averaging over this block. In this paper, an estimate of the observed frequency is performed for each second of data, Let N represent the number of samples per second as shown in Fig 3 and expressed as,

$$y = x[j], \text{ where, } j = 0,1, \ldots . . N - 1, \tag{2}$$

Let $\omega(n)$ represent a window, where $n = 0,1, \ldots M - 1$, and the number of blocks in N number of samples is K shown in Fig. 3. The m-th windowed, zero-padded frame from the signal x can be expressed as,

$$x_m(n) = \omega(n)x(n + mR), , m = 0,1, \ldots K - 1. \tag{3}$$

Where R is defined as the window hop size. The periodogram of the m-th block is given by,

$$P_{x_m,M}(\omega_k) = \frac{1}{M}\left|FFT_{N,k}(x_m)\right|^2 = \frac{1}{M}\left|\sum_{n=0}^{M-1} x_m(n)\, e^{-j2\pi nk/N}\right|^2 \tag{4}$$

From this, the Welch estimate of the power spectral density is given by,

$$\hat{S}_x^W(\omega_k) = \frac{1}{K}\sum_{m=0}^{K-1} P_{x_m,M}(\omega_k) \tag{5}$$

Using the Welch method there is a tradeoff between bias and variance, where the following expression must hold,

$$N \geq (K - 1)R + M \tag{6}$$

If no overlap is implemented ($R = M$), maximum independence is achieved where,

$$N \geq KM \tag{7}$$

The bias of the output depends on the value of K and the variance depends on M. By increasing the block size M, the spectral resolution can be maximized.

In applying the Welch method and detecting the peak for the observed frequency,f_o, the value of M, the block size, plays the main role. The prior information on data rate and the type of modulation are the main factors to determine the value of M. For a low data rate, small bandwidth signal, the value M should be large to enable higher resolution and improved signal to noise ratio. For example, an ASK modulated / CW signal usually has very low data rate where the higher value of M can be used to resolve an accurate peak with great SNR using the peak finding algorithm which is shown in Fig. 3(a). The similar M value can also be chosen for FSK modulated signal as shown in Fig. 3(b). However, for PSK, the high data rate signal causes frequencies to spread over a larger bandwidth, therefore, by lowering the value of M the peak detection algorithm can resolve the center peak of the band. Fig. 3 (c) shows the different outputs to the peak finding algorithm for large and small values of M.

3.2 Angle of Arrival Analysis

In a passive RF system, it is possible to use an antenna array to estimate a satellite's azimuth (ϕ) and elevation (θ) or the AoA relative to the sensor array. The AoA estimation in this paper is performed by the interferometer technique and the Multiple Signal Classification (MUSIC) algorithm. To deploy the AoA algorithms on real data, an L-shaped antenna array was designed as shown in Fig. 4.

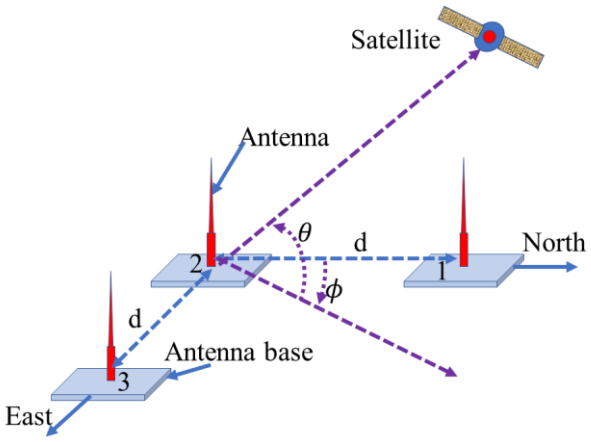

Fig. 4. AoA estimation using an L-shaped planar antenna array

3.2.1 Interferometer Technique

In this paper, an L-shaped planar antenna array, which is shown in Fig. 4, is proposed to apply the interferometer technique [15] to estimate the angle of arrival of the satellite transmitter from the received satellite signals. Three omni directional antennas are placed in three corners of an L-shaped structure. The L-shaped structure is placed parallel to the ground with one arm in the North direction and the other in the East direction as shown in Fig. 4. Antennae 1 and 3 are placed in North and East corners, respectively. Antenna 2 is placed in the middle corner. Let the distance between antenna 1 and 2 be d_{12} and antennae 3 and 2 be d_{32}. For the simplification of the calculations, let d_{12} and d_{32} be equal and represented by d , i.e., $d_{12} = d_{32} = d$. To avoid phase ambiguity, the maximum spacing between antennas should be less than half a wavelength, i.e.,

$$d_{max} = {}^{1}/_{2}\ \lambda\,, \tag{8}$$

where $\lambda = 1/f_0$ and f_0 is the observed frequency.
Let the azimuth and elevation of the satellite signal be ϕ and θ. From, Fig 4, the phase difference between the signals in antenna 1 and 2 can be written as,

$$\gamma_{12} = \frac{d_{12}\,2\,\pi}{\lambda}\cos(\theta)\cos(\phi) \tag{9}$$

Again, the phase difference between antenna 2 and 3 can be written as,

$$\gamma_{32} = \frac{d_{32}\,2\,\pi}{\lambda}\cos(\theta)\sin(\phi) \tag{10}$$

From Equations (9) and (10), the azimuth (ϕ) and elevation (θ) can be derived as follows:

$$\phi = tan^{-1}\left(\frac{\gamma_{32}d_{12}}{\gamma_{12}d_{32}}\right) \tag{11}$$

$$\theta = cos^{-1}\left(\frac{\gamma_{12}\,\lambda}{2\pi d_{12}\cos(\phi)}\right) \tag{12}$$

3.2.2 Multiple Signal Classification Algorithm

MUSIC is a common algorithm used for AoA estimation. It is based on the analysis of signal and noise spaces for the received signal and makes use of the orthogonality between the spaces to search for the AoA [16]. When only one source is assumed, the received signal can be expressed as

$$\boldsymbol{y} = \boldsymbol{e}x + \boldsymbol{n}, \tag{13}$$

where $\boldsymbol{y}$, $\boldsymbol{e}$, x and $\boldsymbol{n}$ denote the received signal, the steering vector, the signal received at the reference point and the additive noise, respectively. Note that $\boldsymbol{y}$, $\boldsymbol{e}$ and $\boldsymbol{n}$ are vectors with dimensions equaling the number of sensors, N_s. In order to implement MUSIC algorithm, the following assumptions are made [17]:

(a) Signal x is zero-mean with power $E|x|^2 = P$. It is independent to the additive noise.
(b) The noise vector $\boldsymbol{n}$ is zero-mean with independent elements, i.e., the additive noise in the sensors is independent.
(c) The noise power, σ^2, is the same, but not necessarily available, for all the sensors.

Note that assumptions (a) and (b) are general in wireless communications systems. Assumption (c) is applicable in most multi-antenna receivers. When the assumptions (b) and (c) do not hold in specific cases, the correlation matrix of the noise will then be needed to whiten the signal.

Under the assumptions made above, the covariance matrix of the received signal can be expressed as

$$\boldsymbol{R_y} = P\boldsymbol{e}\boldsymbol{e}^H + \sigma^2\boldsymbol{I}\,. \tag{14}$$

As the term, $P\boldsymbol{e}\boldsymbol{e}^H$, is a Hermitian matrix with a unit rank, we can see that $\boldsymbol{e}$ is one of its eigenvectors. To verify this, we multiply $P\boldsymbol{e}\boldsymbol{e}^H$ with $\boldsymbol{e}$ to have

$$P\boldsymbol{e}\boldsymbol{e}^H\boldsymbol{e} = (P\boldsymbol{e}^H\boldsymbol{e})\boldsymbol{e}. \tag{15}$$

Eq. 15 also indicates that the eigenvalue corresponding to $\boldsymbol{e}$ is $P\boldsymbol{e}^H\boldsymbol{e}$. As the rank of $P\boldsymbol{e}\boldsymbol{e}^H$ is one, the rest of its eigenvalues are zero. The corresponding eigenvectors can be expressed as $\boldsymbol{v}_1, \ldots, \boldsymbol{v}_{N-1}$, which leads to

$$P\boldsymbol{e}\boldsymbol{e}^H\boldsymbol{v_i} = \boldsymbol{0}, \text{for } i = 1, \ldots, N_s - 1, \tag{16}$$

where $\boldsymbol{0}$ denotes the all-zero vector.

It is straightforward to prove that $\boldsymbol{e}$ and $\boldsymbol{v_i}$ are also eigenvectors of $\boldsymbol{R_y}$. To verify this, we can see that

$$\boldsymbol{R_y e} = (P\boldsymbol{e}\boldsymbol{e}^H + \sigma^2\boldsymbol{I})\boldsymbol{e} = (P\boldsymbol{e}^H\boldsymbol{e} + \sigma^2)\boldsymbol{e} \tag{17}$$

and

$$\boldsymbol{R_y v_i} = (P\boldsymbol{e}\boldsymbol{e}^H + \sigma^2\boldsymbol{I})\boldsymbol{v_i} = \sigma^2\boldsymbol{v_i} \tag{18}$$

The corresponding eigenvalues are $P\boldsymbol{e}^H\boldsymbol{e}$ and σ^2, respectively. In the statistical signal processing literature, the space spanned by $\boldsymbol{e}$ is defined to be the signal space, and $\boldsymbol{v}_1, \ldots, \boldsymbol{v}_{N-1}$, the noise space. The two spaces are orthogonal to each other.

Eq. 18 indicates that

(a) The noise power, σ^2, can be estimated by averaging the smallest $N_s - 1$ eigenvalues.
(b) The steering vector $\boldsymbol{e}$ can be estimated by using the eigenvector corresponding to the largest eigenvalue.

Eq. 17 indicates that after the noise power and steering vector are estimated, the signal power, P, can be estimated from the largest eigenvalue.

When MUSIC algorithm is implemented for AoA estimation, the relationship between the AoA and steering vector $\boldsymbol{e}$ is typically assumed known and depends on the geometry of the sensor array. For example, based on the configuration of the sensors as shown in Fig. 4, the steering vector is given by

$$\boldsymbol{e} = \left[e^{j\frac{2\pi d_{12}}{\lambda}\cos\theta\sin\phi}, \quad 1, \quad e^{-j\frac{2\pi d_{32}}{\lambda}\cos\theta\cos\phi}\right]^T \tag{19}$$

where θ and ϕ denote the elevation and azimuth angles, respectively.

As the covariance matrix, $\boldsymbol{R_y}$, is Hermitian, the steering vector $\boldsymbol{e}$ is orthogonal to the rest of the eigenvectors, $\boldsymbol{v}_1, \ldots, \boldsymbol{v}_{N-1}$. This forms the theoretical foundation of MUSIC algorithm. If forming a matrix $\boldsymbol{V}$ that is made up from the vectors, $\boldsymbol{v}_1, \ldots, \boldsymbol{v}_{N-1}$, i.e., $\boldsymbol{V} = [\boldsymbol{v}_1, \ldots, \boldsymbol{v}_{N-1}]$, then we can form the spatial spectrum, given by $1/\boldsymbol{e}^H\boldsymbol{V}\boldsymbol{V}^H\boldsymbol{e}$. The MUSIC algorithm then performs a search for the elevation and azimuth angles that lead to the maximum spatial spectrum.

4. SATELLITE SIGNAL CAPTURING

Clearbox Systems has a passive RF sensor network across Australia. Satellite signals are captured from two sites which are in Canberra (-35.292062,149.165202) and Adelaide (-35.106667, 138.518993), Australia. Those sites have the capability for a range of frequency bands. Only the VHF and UHF capabilities have been used to capture signals for this paper. They satellites included amateur radio satellites and an ILRS satellite named SARAL. The satellites are listed in Table I, along with the transmitter information for each satellite. The signal from these satellites were used to verify the Doppler and AoA estimation. The satellites were selected as they transmit signals using different modulation techniques.

TABLE I: The list satellites and their on-board features.

Satellite Name	Norad Id	Transmitter			
		Modulation	Signal	Frequency (MHz)	Data Rate
Max Valier Sat	42778	ASK	Telemetry	145.961	12 baud
FALCONSAT-3	30776	FSK	Transceiver	435.103	9k6
NAIF-1	42017	BPSK	Telemetry Beacon	145.940	1k2
SARAL	39086	BPSK PMT-A3	Telemetry	465.988	800 baud

N.B.: PMT-A3: Platform Messaging Transceiver-Argos-3, SARAL is one of the ILRS satellites.

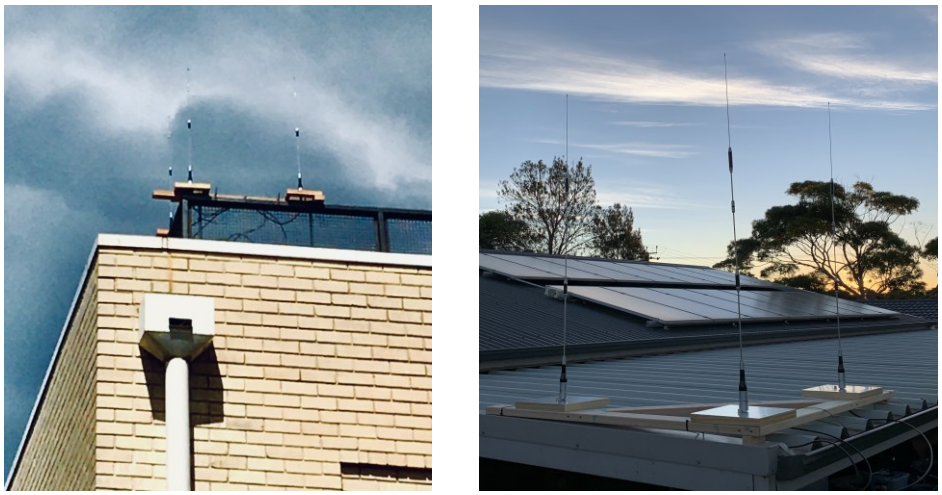

(a) Canberra site (b) Adelaide site

Fig. 4. L-shaped planar antenna arrays for Angle of Arrival (AoA)

The L-shaped VHF/UHF antenna arrays are shown in Fig. 4. Three SG-7900 omni directional antennas are used in the antenna array. The antennas are connected to three channels of a four channel SDR (USRP x310) at each site. Each channel is sampled at 500 kHz.

5. RESULTS AND ANALYSIS

Doppler and AoA are estimated based on theory explained in section 3. Doppler is estimated for ASK, FSK and PSK modulated signals and compared with TLE and ILRS data. On the other hand, AoA is estimated only for ASK modulated signal and compared with TLE data. The satellites whose signals are used for the analysis are tabulated in Table I.

5.1 Doppler Estimation

The observed frequency and the Doppler frequency are estimated for the ASK modulated signal from Max Valier Sat as listed in Table I. The data is captured from the Adelaide site for the pass starting at 2021-06-04T22:16:40Z and ending at 2021-06-04T22:24:07Z. For each estimation, 500,000 samples are taken which is equal to the sample rate, i.e., $N = 500k$. For this type of modulation, a block size of $M = 25000$ was used with no overlap considered, $R = M$. The estimated Doppler is compared with the derived Doppler from the TLE. The estimated Doppler is shown in Fig. 5 along with the Doppler derived from the TLE. The difference between the estimated and derived Doppler shifts are represented as a Doppler error also shown in Fig. 5. The root mean square (RMS) of Doppler error for the duration of the capture is 3.04 Hz. It is observed from the figure that the mean of Doppler errors are non-zero and changing over time, which is possibly due to the TLE error, as explained in section 5.1.1.

The observed frequency and the Doppler are estimated for an FSK modulated signal from FALCONSAT-3 as listed in Table I. The data was captured from the Canberra site for the pass starting at 2021-03-07T23:22:52Z and ending at 2021-03-07T23:31:59Z. For each estimation, 500,000 samples are taken which is equal to the sample rate, i.e., $N = 500k$. For this type of modulation, a block size of $M = 2000$ was used with no overlap considered, $R = M$. The estimated Doppler is compared with the derived Doppler from the TLE. The estimated Doppler is shown in Fig 6 along with the Doppler derived from the TLE. The difference between the estimated and derived Doppler shifts are represented as the Doppler error shown in Fig. 6. The RMS of Doppler error for the duration of the capture is 66.55 Hz. For each estimation, the two peaks of the FSK carriers are first estimated then the center frequency is calculated.

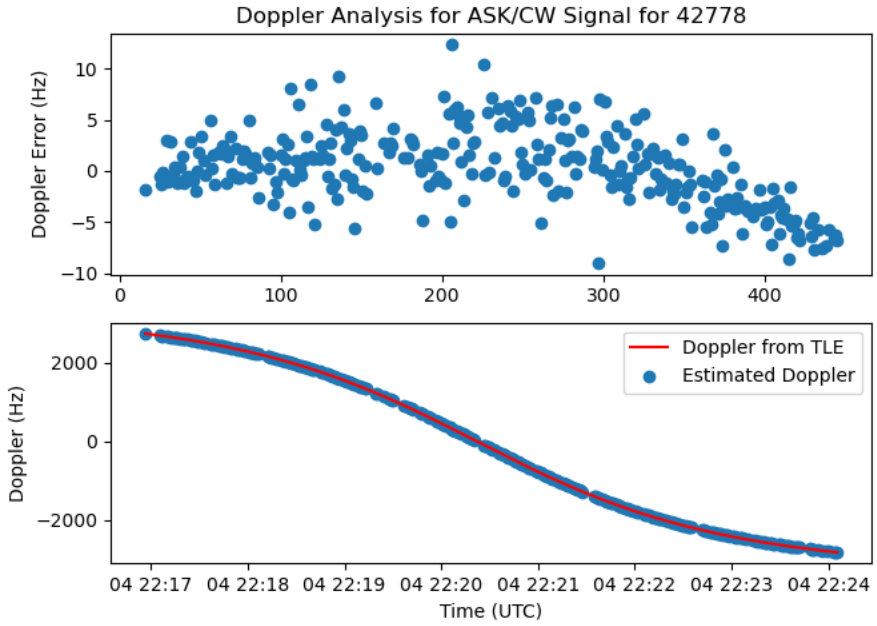

Fig. 5. Estimated Doppler and error compared to the TLE for the pass of Max Valier Sat starting at 2021-06-04T22:16:40Z and ending at 2021-06-04T22:24:07Z captured from the Adelaide sensor site.

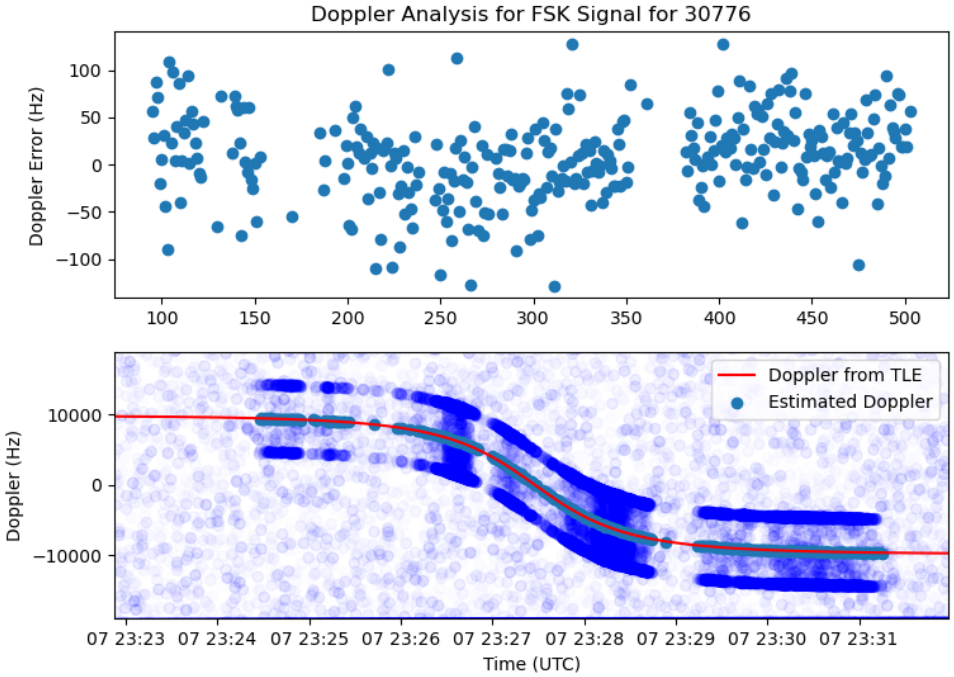

Fig. 6. Estimated Doppler and error compared to the TLE for the pass of FALCONSAT-3 starting at 2021-03-07T23:22:52Z and ending at 2021-03-07T23:31:59Z captured from the Canberra sensor site.

The observed frequency and the Doppler are estimated for PSK modulated signal from NAIF-1 as listed in Table I. The data is captured from the Canberra site for the pass starting at 2021-03-10T12:43:03Z and ending at 2021-03-

10T12:51:52Z. For each estimation, 500,000 samples are taken which is equal to the sample rate,

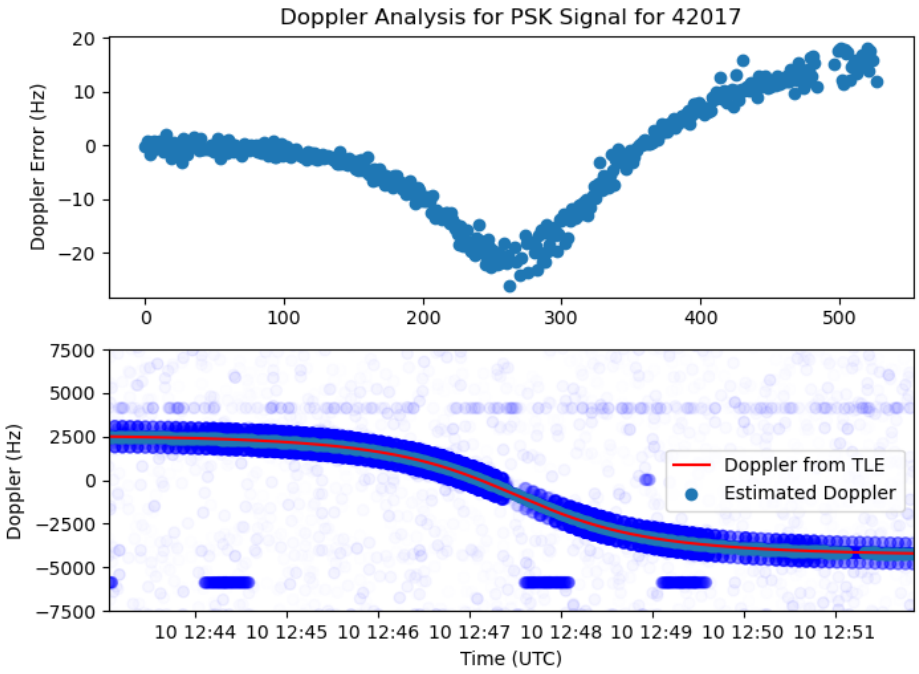

Fig. 7. Estimated Doppler and error compared to the TLE for the pass of NAYIF-1 starting at 2021-03-10T12:43:03Z and ending at 2021-03-10T12:51:52Z captured from the Canberra site.

i.e., $N = 500000$. For this type of modulation, a block size of $M = 8000$ was used with no overlap considered, $R = M$. The estimated Doppler is compared with the derived Doppler from the TLE. The estimated Doppler is shown in Fig 7 along with the Doppler derived from the TLE. The difference between the estimated and predicted Doppler shifts is represented as the Doppler error in Fig. 7. The RMS value of Doppler error for the duration of the capture is 10.06 Hz. The variation of mean with time is due to the error in TLE which is later analysed comparing the estimates with accurate ILRS data. From Fig. 7, it is clear that the estimated Doppler follows the center frequency of the frequency band.

5.1.1 Comparison with ILSR data:

Signal from one of the International Laser Ranging Service (ILRS) satellites, SARAL, was captured from the sensor sites to compare the Doppler to highly accurate ephemeris data. The signal captured from the Adelaide site for the pass starting at 2021-05-24T20:00:37Z and ending at 2021-05-24T20:11:28Z is used to estimate the Doppler. For each estimation, 500,000 samples are taken which is equal to the sample rate, i.e., $N = 500{,}000$. For this modulation type a block size of $M = 13000$ was used with no overlap considered, $R = M$.

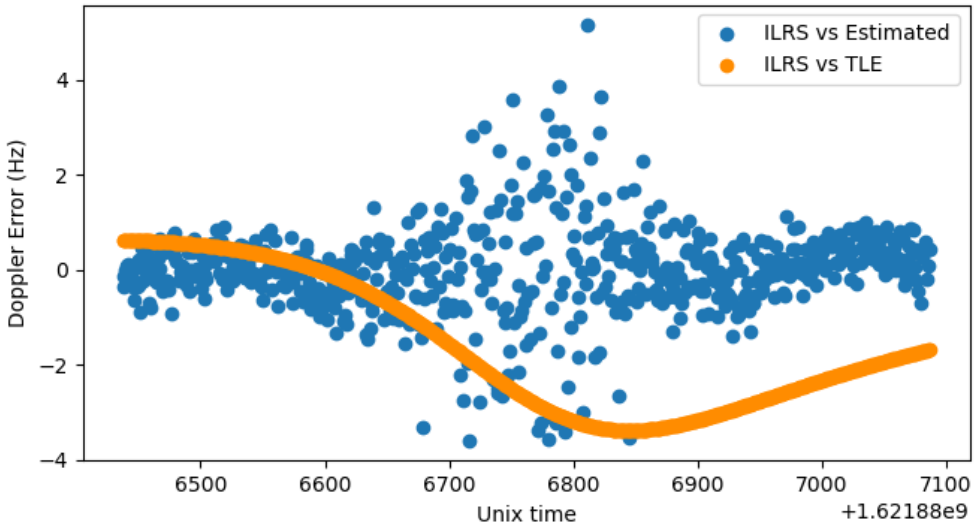

Fig. 8. Doppler comparison among ISLR, TLE and estimated for SARAL for the pass started at 2021-05-24T20:00:37Z and ended at 2021-05-24T20:11:28Z from the Adelaide site.

The estimated Doppler and the calculated Doppler from the TLE are compared with the highly accurate Satellite Laser Ranging (SLR) data provided by ILRS. The Doppler errors are shown in Fig. 8. The mean and standard deviation of the Doppler estimates compared to the ILRS ephemeris are 0 Hz and 0.9 Hz respectively. When comparing the TLE to the ILRS ephemeris the mean and standard deviation are-1.5814 Hz and 1.4159 Hz respectively. Based on this result, the estimated Doppler is found to be more accurate than the given TLE. The estimated Doppler variation is less and in the range of fraction of a hertz in the beginning and end of the pass while in the range of ± 4 Hz in the middle of the pass due to the rate of change of Doppler being its highest during the middle of the pass.

From this comparison with accurate SLR data, it has been demonstrated that the estimated Doppler from this method is more accurate than the given TLE. When comparing the Doppler estimates with the TLE shown in Figs 5 and 7 the means of the Doppler errors were varying with time. This analysis has indicated that this is due to TLE errors.

5.2 AoA Estimation

Both interferometer method and MUSIC algorithm have been implemented to estimate the azimuth (ϕ) and elevation (θ) of a satellite signal. The AoA estimation is carried out for ASK modulated signal from Max Valier Sat as listed in Table I. The three antennas of the array were connected to three channels of the SDR. The SDR channels are phase synchronised and the phases for three RF chains from the antenna to the SDR are calibrated prior to digitising the satellite signals to IQ data. The satellite signal is captured for the pass starting at 2021-06-04T22:16:40Z and ending at 2021-06-04T22:24:07Z.

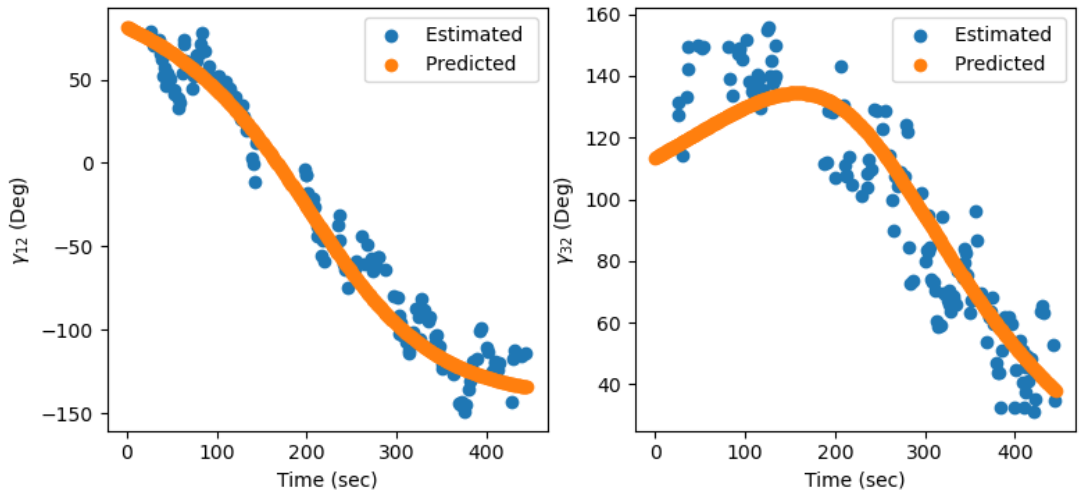

Fig. 9. Phases estimation and compared to the TLE for the pass of Max Valier Sat starts at 2021-06-04T22:16:40Z and ends at 2021-06-04T22:24:07Z

In the interferometer method, the phase differences between antennas 1 and 2 and antennas 2 and 3 are estimated in two ways: (a) using cross-correlation method in time domain and (b) using the FFT magnitude and phase information for the observed frequency. The estimated phases and the predicted phases from given TLE are shown in Fig. 9. The RMS errors compared to the TLE for γ_{12} and γ_{32} are calculated of 13.6 and 14 degrees, respectively. These angles are used to estimate the azimuth (ϕ) and elevation (θ) based on the equations (11) and (12) which are shown in Fig. 10. The RMS errors of azimuth (ϕ) and elevation (θ) compared to TLE are 5.5 and 8.7 degrees, respectively.

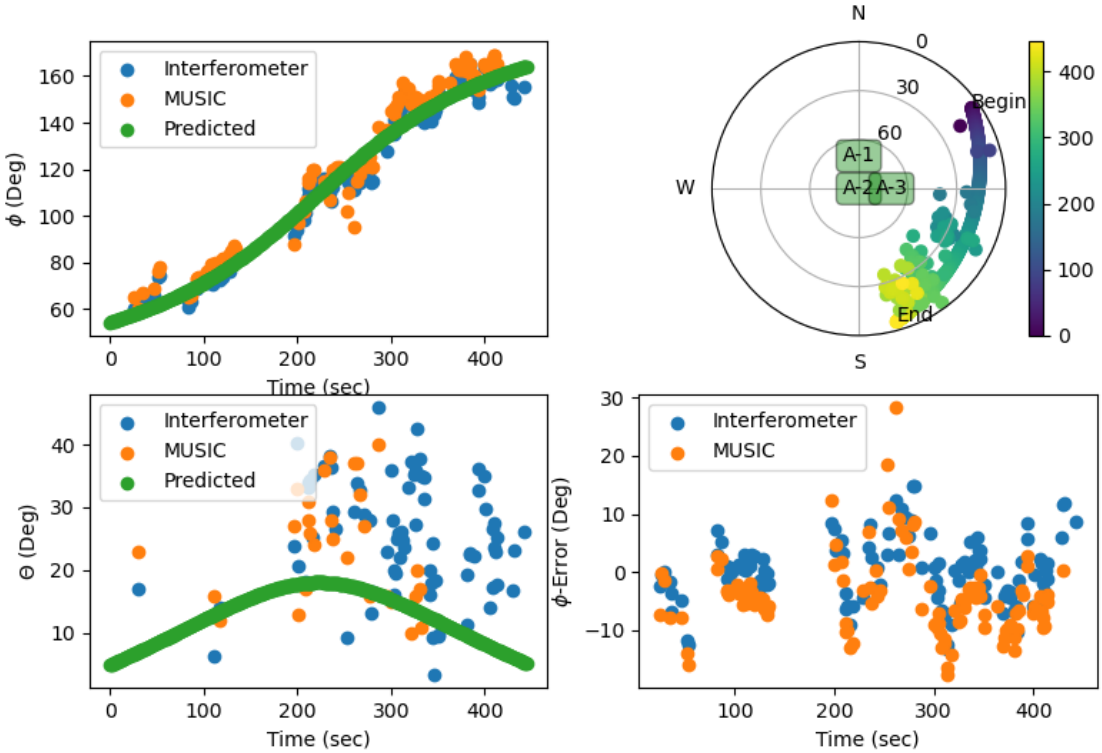

Fig. 10. AoA estimation and compared to the TLE for the pass of Max Valier Sat starts at 2021-06-04T22:16:40Z and ends at 2021-06-04T22:24:07Z

Again, the azimuth and elevation angles are directly estimated using the MUSIC algorithm. The signal is filtered with a bandpass filter of 200 Hz bandwidth around the observed frequency, f_0 , i.e., $f_o \pm 100$, where f_o is estimated by welch method as explained in section 5.1, The covariance matrix, $\boldsymbol{R_y}$, used in MUSIC algorithm is estimated as expressed in eq. 14. The estimated azimuth (ϕ) and elevation (θ) by MUSIC algorithm are shown in Fig. 10. The RMS azimuth and elevation errors compared to TLE are 6.7 and 7.9 degrees, respectively.

The results shown in Fig. 9 and 10 demonstrate that both interferometer and MUSIC algorithm are feasible techniques for AoA estimation for LEO satellites and either method could be used for AoA estimation for ASK modulated signal. From the Fig. 10, it is observed that the estimated azimuth is close to the predicted value, but the elevation is more erroneous.

The AoA estimation uses signals from three antennas. Therefore, in AoA estimation, antennas, amplifiers, and cables need to be identical, all the channels in the SDR need to be phase synchronised and each of the three antennas in the array should receive signal equally. Again, AoA estimation is also sensitive to the mutual coupling between antennas as it impacts the voltage induction in all three antennas. The errors in AoA arises may have different reasons, such as

(a) all the off-the-shelf components are used in the AoA experiment, which may not be identical,
(b) different mutual coupling between antennas as the distance among antennas are not equal,
(c) the orientation of the antenna in Max Valier Sat may changing over time,
(d) the signal to noise ratio (SNR) was not constant over the pass,
(e) multiple path fading may happen,
(f) some terrestrial signals are noticed in the frequency range in Adelaide site, and
(g) antenna array is constructed with minimum number of antennas and place horizontally on 2D-plane.

Some of these reasons have been investigated prior to the data being captured, however, the other reasons need more investigation.

6. CONCLUSION AND FUTURE WORK

This paper describes and implements the Welch method in determining the Doppler for LEO satellites from their signals consisting of a variety of modulation techniques. The accuracy of the estimated Doppler is found to be less than a Hz compared to the accurate ILRS satellite laser ranging data. An L-shaped planar antenna array is proposed for AoA estimation. Both the interferometer technique and MUSIC algorithm are applied to AoA determination for an ASK modulated satellite signal. The estimated AoA is compared with the predicted AoA calculated from the TLE. Future work will look to improve the accuracy of AoA estimation by increasing the number of antennas in the array and by vertical placement of the array. The AoA estimation will also be extended to PSK and FSK modulated satellite signals. Using the Doppler and AoA measurements orbit determination will also be investigated in future work.

7. ACKNOWLEDGEMENT

This research was conducted as part of an Australian Cooperative Research Centre Projects (CRC-P) led by Clearbox Systems in collaboration with the University of New South Wales (UNSW). The authors would like to acknowledge the support from the Australian Department of Industry, Science, Energy and Resources as well as the support from UNSW Canberra for hosting a sensor site to enable real data to be collected.

8. REFERENCES

[1] https://www.cnbc.com/2021/01/24/spacex-launches-rideshare-mission-with-143-spacecraft.html, cited on August 26, 2021.

[2] https://www.sda.mil/us-military-places-a-bet-on-leo-for-space-security/, cited on August 26, 2021.

[3] https://www.kratosdefense.com/

[4] Matthew Prechtel, "Event Detection from RF Sensing." 34th Space Symposium, Technical Track, Colorado Springs, Colorado, United States of America, April, 2018.

[5] Kameron Simon, "Passive RF in Support of Closely Spaced Objects Scenarios", In Advanced Maui Optical and Space Surveillance (AMOS) Technologies Conference, September 2020.

[6] Lal, Bhavya, et al. "Global trends in space situational awareness (SSA) and space traffic management (STM)." Science and Technology Policy Institute (2018).

[7] Morreale, Brittany, Travis Bessell, Mark Rutten, and Brian Cheung. "Australian Space Situational Awareness Capability Demonstrations." In Advanced Maui Optical and Space Surveillance (AMOS) Technologies Conference, p. 63. 2017.

[8] Square Kilometre Array. 2018. "Participating Countries." https://www.skatelescope.org/participating-countries/

[9] Islam, Mohd Noor, Tim Spitzer, Jeremy Hallett, and Md Asikuzzaman. "Doppler Estimation for Passive RF Sensing Method in Space Domain Awareness." In 2020 Military Communications and Information Systems Conference (MilCIS), pp. 1-4. IEEE, 2020.

[10] http://mdkenny.customer.netspace.net.au/ARGOS-3.pdf, cited on August 26, 2021.

[11] P. D. Welch, "The use of fast Fourier transforms for the estimation of power spectra: A method based on time averaging over short modified periodograms," IEEE Transactions on Audio and Electroacoustics, vol. 15, pp. 70-73, 1967

[12] https://www.space-track.org/, cited on August 26, 2021.

[13] https://cddis.nasa.gov/, cited on August 26, 2021.

[14] "Introduction into Theory of Direction Finding," Rohde & Schwarz Radio monitoring & Radiolocation, Catalog 2010/2011

[15] Guo, Fucheng, Yun Fan, Yiyu Zhou, Caigen Xhou, and Qiang Li. Space electronic reconnaissance: localization theories and methods. John Wiley & Sons, 2014.

[16] R. O. Schmidt, "Multiple Emitter Location and Signal Parameter Estimation," IEEE Transactions on Antennas and Propagation, vol. AP-34, no. 3, pp. 276-280, Mar. 1986.

[17] P. Stoica and A. Nehorai, "MUSIC, Maximum Likelihood, and Cramer-Rao Bound," IEEE Transactions on Acoustics, Speech, and Signal Processing, vol. 37, no. 5, pp. 720-741, May 1989.